electronics

MDPI

Article

Ultra-Wideband Reconfigurable X-Band and Ku-Band Metasurface Beam-Steerable Reflector for Satellite Communications

David Rotshild * and Amir Abramovich

Department of Electrical and Electronic Engineering, Ariel University, Ariel 407000, Israel; amir007@ariel.ac.il
* Correspondence: drotshild@gmail.com

Abstract: A continuously reconfigurable metasurface reflector based on unit cell mushroom geometry that was integrated with a varactor diode is presented in this paper. The unit cell of the metasurface was designed and optimized to operate in the X-band and Ku-band, improving satellite communication's quality of service. The losses mechanisms of continuous control over the unit cell phase reflection in beam steering resolution are considered and the analysis results are presented. The unit cell design parameters were analyzed with an emphasis on losses and dynamic reflection phase range. The unit cell magnitude and phase reflection are shown in the wide frequency bandwidth and showed a good agreement between all the measurements and the simulations. This metasurface enabled a high dynamic range in the unit cell resonant frequency range from 7.8 to 15 GHz. In addition, the reflection phase and absorption calibration are demonstrated for multiple operating frequencies, namely, 11 GHz, 12 GHz, and 13.5 GHz. Furthermore, design trade-offs and manufacturing limitations were considered. Finally, a beam-steering simulation using the designed metasurface is shown and discussed.

Keywords: beam steering; Ku-band; metasurface; tunable circuits and devices

Citation: Rotshild, D.; Abramovich, A. Ultra-Wideband Reconfigurable X-Band and Ku-Band Metasurface Beam-Steerable Reflector for Satellite Communications. *Electronics* **2021**, *10*, 2165. https://doi.org/10.3390/electronics10172165

Academic Editor: Mauro Tropea

Received: 28 July 2021
Accepted: 31 August 2021
Published: 4 September 2021

1. Introduction

The reconfigurable metasurface (MS) field has grown dramatically in recent years, with many MS studies in various frequencies and methods for different applications [1–5]. MS is a private case of a metamaterial in which a surface configuration containing a two-dimensional (2-D) array of cyclic or semi-cyclic unit cells smaller than the operating wavelength. This spatial arrangement gives the material properties at the macroscopic level that do not exist directly in its natural structure. Like ordinary homogeneous materials composed of atoms at the microscopic level, the "new" material comprises individual unit cells, which are meta-atoms at the microscopic level [6,7]. Since the periodic meta-atomic structure functions as "atoms" in a homogeneous material, the wavelength of the relevant radiation must be greater than the "meta-atomic" dimensions. The larger the wavelength relative to the meta-atom, the higher the uniformity of the homogeneous material property at the macroscopic level. MS is used in nanotechnology, radar, antennas, optical lenses, and more [1–5]. Adding a tunable element to the MS unit cells enables a wide range of applications, such as a reconfigurable beam-steering reflector [8], reflective surface that functions as a parabolic mirror with an adjustable focus [9], and more [1–5]. The common MS unit cell type is the resonant unit cell [8]. Around the unit cell resonance frequency f_{res}, the unit cell reflection phase values change significantly. Thus, changing the f_{res} around the operating frequency enables a high dynamic phase range at the operating frequency. The ability to continuously control and reconfigure the reflection phase value's distribution throughout the MS reflector allows for creating an appropriate reflection phase petrean on the MS. This enables reflected beam steering. This approach is called phase-gradient MS [10]. However, a major barrier to adopting MS solutions is the relatively high losses that are associated with the resonant characteristic of the unit cell. There are two mains

loss mechanisms in the MS applications based on continuous control over the reflection phase values of the unit cell:

(1) Phase errors resulting from the dynamic reflection phase range of less than 360°.
(2) The unit cell resistance R causes losses, mainly at phase values around the f_{res}.

The chosen method for tuning capability parameter is defined as TC and the parameter of the unit cell Q-factor as Q. The unit cell dynamic reflection phase range is proportional to $TC \times Q$; therefore, a small TC can be compensated by increasing the Q. It also increases unit cell losses proportional to $R \times Q$ [11]. On the other hand, a large TC allows for a reduction in Q and unit cell losses while maintaining a high dynamic phase reflection range. Several methods add reconfiguring and tuning to MS, such as PIN switches, MEMS switches, liquid crystal materials, piezoelectric materials, and varactor diodes [8,9,12–22]. The liquid crystal method is used in the K-band and above and can be realized in MS as a tuning dielectric substrate, without any external element in the front, but is more challenging to implement [16]. The dielectric constant is the fundamental parameter, which changes in the liquid crystal tuning method. This parameter varies slightly in the order of tens of percent with a relatively low TC. Thus, increasing the Q of the unit cell compensates for the inherent low tunability and allows for a significant dynamic phase range, but increasing Q also increases the losses, frequency dispersion, sensitivity to tolerances, and decreases bandwidth [16]. The liquid crystal has a slow response time, which is slower than the diode varactors' and switches' response times by several orders of magnitude [23]. Thus, liquid crystal is less suitable for continuous tracking and switching applications. Piezoelectric microelectromechanical system (MEMS) materials enable continuous changes in the unit cell thickness depending on the DC voltage [12,22]. Thus, the properties of the MS continuously change as well. Using the piezo MEMS method is limited because it involves a physical change in the unit cell size. In addition, a high voltage of up to 200 V is needed for the control [22]. Several methods of tuning for digital coding MS applications are with quantization control over the unit cell reflection phase, mainly switches. The PIN switch enables frequency work up to 70 GHz, with a fast switching time, high reliability, low cost, and low control voltage of switches for digital coding MS applications with quantization control over the unit cell reflection phase [24,25]. Recently, the MEMS switch aroused attention due to its small size and linearity [26,27], but it has a relatively slow switching time compared to the PIN switch [24]. In addition, many switch components operate at voltage levels of 0 V and 5 V, which are standard voltages for controllers and electronic components that simplify the realization of the DC biasing circuit. However, the discrete nature of the switch state prevents the switches from being used in applications where a continuous phase change is required. The switches do not meet our basic requirement since it is impossible to achieve high-resolution beam steering, let alone the possibility of continuous tracking for surfaces that are not unusually large.

A varactor diode allows for a continuous and high-tuning-capacitance ratio and fits the continuous reflection phase method in the proposed MS reflector [8,14,15,17–19,28–30]. The varactor diodes allow for high-frequency work up to 70 GHz, a conventional PCB assembly, and extremely low consuming power [31], and thus leads to a focus on the varactor diode in this study. However, the varactor diode suffers from relatively high losses compared to the switches. The losses effect is reduced by decreasing Q [11,17–19]. The reduction in Q is justified due to the very high tunability of the varactor diode capacitance value with a high TC parameter. In addition, using the quantization reflection phase method compared to the continuous reflection phase method adds quantization losses for beam steering of about 4 dB for 1-bit digital coding MS and about 1 dB for 2-bit digital coding MS [32,33]. Thus, considering the total losses budget for a beam-steering application, using the varactor diode seems better, but additional research is required. Therefore, considering the total losses budget for a beam-steering application, using the varactor diode seems better, but further research is required.

A reconfigurable MS reflector based on varactor diodes as a tuning element is well known with many published implementations operating at frequencies of up to

6 GHz [8,15,28,29], with very few at X-band and above [18,30,34], where one of them [34] is categorized as a sparse MS and not as a classic MS. Such implementations in the X-band and above will improve satellite communications' quality of service (QoS) in the X-band and Ku-band [35]. Furthermore, an MS reflector with a high range and accurate beam steering enables the coverage of shaded areas and improved quality of service, including beam tracking. Such continuously reconfigurable MS reflectors for high-resolution beam steering operating above the X-band frequency are needed to improve satellite communication.

However, the implementation of reconfigurable MS above the X-band, based on a varactor diode as a tuning element, is challenging due to the constraint to reduce unit cell dimensions and increasing the diodes' density on the surface while maintaining the performance. In addition, the varactors require many DACs, complicating the realization of the DC biasing circuits in small dimensions.

2. Continuous Beam Steering MS Reflector Concept

The schematic structure of the designed MS reflector and its equivalent electric circuit model are shown in Figure 1.

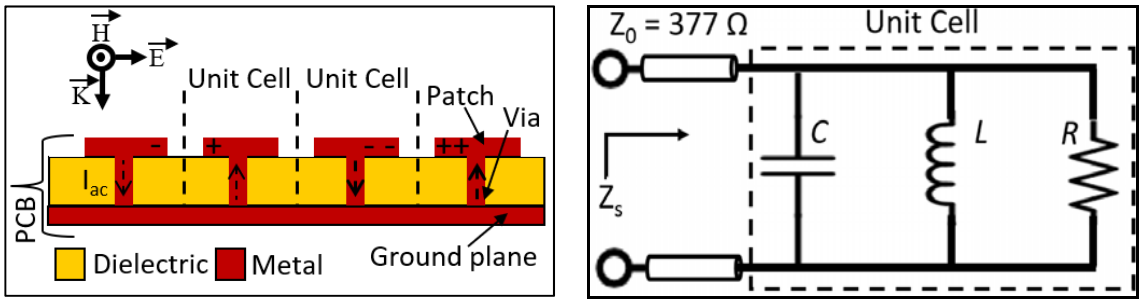

(**a**) (**b**)

Figure 1. MS reflector structure and basic unit cell model: (**a**) side view of the MS structure interacting with a plane wave and (**b**) MS unit cell equivalent circuit model.

Figure 1a shows the basic MS reflector structure composed of a printed metal shape on a dielectric substrate. The printed metal shape on the front side can be a patch, a slot, a ring [1,36], or more complex geometries, such as a K-shape [14], connected via a metal surface used as a ground plane at the backside. Figure 1b presents the equivalent circuit of lumped elements with inductance, capacitance, and resistance components for the destined unit cell [11].

The plane wave electric field component interacts with the patches' edges, arousing surface charges (marked by +/− signs in Figure 1a); this is modeled as a capacitance *C*. The magnetic flux developing from the current (marked by dashed arrows in Figure 1a) between the patch and the ground plane through the via is modeled as an inductance *L*. The dielectric and ohmic losses are modeled as a resistance *R*, which is the dissipation resistive part of the unit cell. When the unit cells are arranged in a 2-D periodic configuration, the surface is characterized as an effective impedance surface, which was defined by Dan Sievenpiper's work [11] with the surface impedance parameter Z_S, which is shown in Equation (1):

$$Z_S = \frac{1}{1/R + j(\omega C - 1/\omega L)} \tag{1}$$

where around the angular frequency values of $\omega = 1/\sqrt{LC}$, the imaginary part of the Z_S becomes dominant, and is shown in Equation (2):

$$Z_S = \frac{j\omega L}{1 - \omega^2 LC} \tag{2}$$

The values of C and L are determined by the unit cell's dimensions, geometry, materials, and PCB properties. The parallel resonance frequency f_{res} of the circuit model around which the radiation is manipulated is shown in Equation (3):

$$f_{res} = \frac{1}{2\pi\sqrt{LC}} \tag{3}$$

The bandwidth of the resonance frequency [37] is shown in Equation (4):

$$BW = \frac{1}{(RC\omega_0)}) = \frac{(L\omega_0)}{R} \propto \frac{L}{C} \tag{4}$$

The Q-factor is shown in Equation (5):

$$Q = \frac{1}{BW} \propto \frac{C}{L} \tag{5}$$

According to the phased array theory, each unit cell location on the MS is defined at its center [38]. A 2-D surface in the XY plane with a spatial array arrangement of a fixed distance and a 90° angle between the unit cells is defined as S (x_j, y_i), $j = 1, 2, \ldots, N$ and $i = 1, 2, \ldots, M$, where N and M are integer numbers that lead to an array of $N \times M$ unit cells. This unit cell array with the desired phase distribution throughout the surface allows for focusing radiation to the desired point [9] or radiation steering to the desired direction [8]. A scheme of a beam-steering side cross-section view that is representative of an MS reflector is shown in Figure 2.

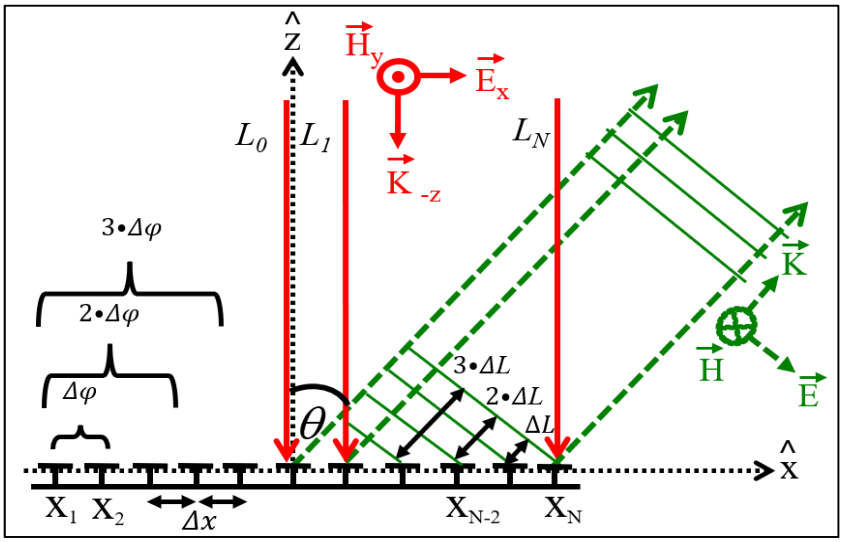

Figure 2. MS reflector side cross-section view scheme of the beam-steering principle.

Figure 2 shows a scheme of radiation steering using an MS reflector, where L_1, L_2, and L_N are incident rays toward the surface marked in red arrows. The optical path difference (OPD) between the reflected rays from unit cells X_j to X_{j+1} is defined as ΔL and is described in Equation (6):

$$\Delta L = \Delta X \sin\theta \tag{6}$$

where ΔX is the array constant. For beam steering, ΔL is constant for all different paths from adjacent cells X_j and X_{j+1} throughout the surface. The conversion of ΔL into a phase difference is shown in Equation (7):

$$\Delta\varphi_x = \frac{360 \cdot \Delta L}{\lambda} \tag{7}$$

where λ is the wavelength at the working frequency. By supplying the accumulated phase difference $\Delta\varphi_x$ from left to right throughout the surface, between adjacent unit cells X_j and X_{j+1} in the x-axis, each reflected ray marked in dashed green arrows gets additional accumulated ΔL. Thus, it leads to the desired steering angle θ in the XZ plane, as shown in Figure 2. Using Equations (6) and (7), the connection between $\Delta\varphi$ and ΔX to the desired angle steering θ is shown in Equation (8):

$$\theta = \sin^{-1}\left(\frac{\lambda \cdot \Delta\varphi_x}{360 \cdot \Delta X}\right) \tag{8}$$

The 2-D periodic structures can be simulated in three-dimensional electromagnetic simulation software, such as HFSS and CST [39]. Due to their importance, there are dedicated simulation solvers that simplify the process and save time. In addition, these solvers enable extracting the surface reflection properties and dispersion diagram from a single unit cell simulation [40].

To illustrate the resolution limit of digital coding metasurface, using the conceptual surface of 16 columns composed of 5 mm unit cells, with 2-bit coding, at an operating frequency of 10 GHz, and a planned beam-steering to $\theta = 1^\circ$ in XZ plane, as defined in Figure 2, is demonstrated. The four-phase state's phase range definition, the desired reflection phase-gradient, and the distribution of the final state are shown in Figure 3.

	0<	φ	≤90		90<	φ	≤180		180<	φ	≤270		270<	φ	≤360	
Unit cell number	1	2	3	4	5	6	7	8	9	10	11	12	13	14	15	16
Phase gradient	0°	1.05°	2.1°	3.15°	4.2°	5.25°	6.3°	7.35°	8.4°	9.45°	10.5°	11.55°	12.6°	13.65°	14.7°	15.75°
Unit cell state																

Figure 3. MS phase and state distribution.

Figure 3 shows the phase value required for the desired beam steering for each unit cell. According to Equation (8), $\Delta\phi = 1.05^\circ$, and the cumulative phase difference is $1.05 \times 15 = 15^\circ$, which is less than 90°. Since all phase values are between 0 and 90°, the entire unit cell surface is set to state '1,' and there is no manipulation of the beam reflection direction. For beam steering of $\theta = 5^\circ$, where $\Delta\phi = 5.23^\circ$ and the cumulative phase difference is $5.23^\circ \times 15 = 78.45^\circ$, there is still no change in the unit cell state. Adding a constant phase to the entire MS that does not affect the phase gradient [13] leads to a maximum of two-phase states for use, as shown in Figure 4.

Unit cell number	1	2	3	4	5	6	7	8	9	10	11	12	13	14	15	16
Phase gradient	0°	1.05°	2.1°	3.15°	4.2°	5.25°	6.3°	7.35°	8.4°	9.45°	10.5°	11.55°	12.6°	13.65°	14.7°	15.75°
Constant phase	82.5°	82.5°	82.5°	82.5°	82.5°	82.5°	82.5°	82.5°	82.5°	82.5°	82.5°	82.5°	82.5°	82.5°	82.5°	82.5°
Final phase	82.5°	83.55°	84.6°	85.65°	86.7°	87.75°	88.8°	89.85°	90.9°	91.95°	93°	94.05°	95.1°	96.15°	97.2°	98.25°
Unit cell state																

Figure 4. MS phase and state distribution using a constant phase.

As shown in Figure 4, the eight unit cells on the left are defined as phase state '1,' and the eight unit cells on the right are defined as phase state '2.' A change in the constant phase value leads to a change in the unit cells states for the same planed phase gradient; therefore, there is no single-valued par unit cell state for a given phase gradient. This

inherent resolution difficulty of the digital coding of an MS reflector can be solved using unit cells, which provide a continuous reflection phase. The phase gradient is applied directly to the unit cells, as shown in Figure 4, line 2.

3. Unit Cell and MS Reflector Concept and Design

The unit cell design was adopted and optimized for the X-band and Ku-band using mushroom geometry combined with a varactor diode. Such an MS structure is also known as a reconfigurable high impedance surface due to its reflection properties compared to a metal surface [36]. The geometry and dimensions of the optimized unit cell and the standard unit cell are shown in Figure 5.

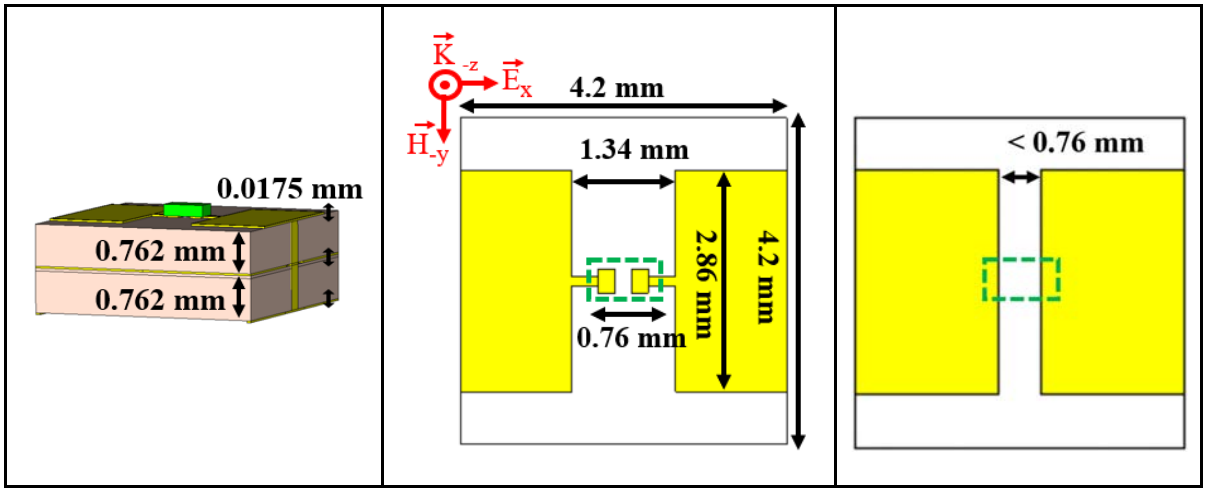

Figure 5. Unit cell design: (**a**) unit cell side view, (**b**) unit cell front side, and (**c**) standard patch unit cell design.

Figure 5a,b shows the unit cell structure, with the varactor diode marked in a green rectangle. The unit cell area sizes are 4.2 mm × 4.2 mm, with a thickness of 1.68 mm. The unit cell sizes in wavelength units are $0.168\lambda_0 \times 0.168\lambda_0 \times 0.065\lambda_0$, where λ_0 is the free-space wavelength at the operation frequency of 12 GHz. The main unit cell dimension parameters are shown in Figure 5a. The unit cell comprises two dielectric substrates of the Rogers company, model 5880LZ, with a thickness of 0.762 mm and a dielectric constant $\varepsilon_r = 2$ [41], and three copper layers (in yellow), each with a thickness of 0.0175 mm. The top copper layer is the square patch. The middle copper layer is for metal ground purposes, separated by a clearance from the via that crosses it. The back-side copper layer is for DC biasing purposes, which is connected by a via with a diameter of 0.3 mm to the top copper layer, thus, to the varactor (shown in Figure 5b).

The unit cell geometry, dimensions, materials, varactor, and the PCB manufacturing process quality determine the total capacitance C and the inductance L. The surface area and the patch size of the unit cell are proportional to the unit cell's intrinsic capacitance C_{int}. The thickness of the dielectric substrate is proportional to the unit cell's intrinsic inductance L_{int} [8,11].

Adding the variable varactor capacitance C_d to the MS changes the total unit cell capacitance C to $C = C_{int} + C_d$. The total unit cell inductance is defined as $L = L_{int}$ for the equivalent circuit model in Figure 1b and Equations (1)–(5).

Reducing the unit cell's dimensions decreases the LC product in Equation (3), which is necessary for high f_{res} values. As shown in Equation (5), reducing C decreases the Q and thus the total unit cell losses $R \times Q$. Therefore, reducing C_{int} values rather than L is required to decrease the LC product in Equation (3), allowing for a high operation frequency. Furthermore, the decrease in C values increases the bandwidth and minimizes the phase errors (see Equation (4)). The unit cell's low capacitance and the high tuning capacitance

ratio are the fundamental requirements for allowing high-frequency implementation of the reconfigurable phase gradient MS reflector with continuous reflection phase control. Following these requirements, a varactor diode of MACOM model MAVR–011020-11411 was chosen as a tuning element. It allows for a continuous and high dynamic range regarding the capacitance value. To the best of our knowledge, this varactor diode has the lowest capacitance in the market. The varactors enable high-frequency operation; a continuous, high-capacitance dynamic range; low power consumption; and simplicity in manufacturing [42]. Decreasing the value of C_{int} makes the value of C_d more dominant in the total unit cell capacitance C and increasing its dynamic tuning range. Using a dielectric substrate with ε_r = 2 and reducing the unit cell and patch sizes reduces the value of C_{int} [11,17–19,36]. The reduction in the patches prevented the varactor from being placed directly on the adjacent patches' edges (blind pad), as in other works [8,15,28,30]. In this design, the distance between the unit cell patches edges was 1.34 mm, while the varactor length dimension is 0.76 mm [42]. This point is demonstrated in Figure 5c. For standard mushroom unit cell configuration, reducing the distance between the patch's edges compared to the varactor length dimension allows the varactor assembly directly on the patches' edges. But, it increased the C_{int}, which impaired the ability and quality of the realization for the X-band frequencies and above. Thus, the varactor diodes were placed between the unit cells' patches on the customized pads according to the layout of the varactor, which required the proper design of vertical lines from the patches to the customized pads, as shown in Figure 5b. To overcome this limitation, the varactor diodes were placed between the unit cells' patches on the customized pads according to the varactor layout, which required the proper design of vertical lines from the patches to the pads, as shown in Figure 5b.

The maximum and minimum values of the diode capacitance for three voltage states (0, 4, and 15 volts) are given in the datasheet without providing a typical value. As a result, there is a non-uniformity in the simulation-defined C_{max} and C_{min} capacitance values in published works that use this diode. For example, in [43], C_{max} = 0.27 pF and C_{min} = 0.032 pF; in [44], C_{max} = 0.19 pF and C_{min} = 0.025 pF; and in [45], C_{max} = 0.25 pF and C_{min} = 0.033 pF. These varactor capacitance values are critical for design considerations. Therefore, for reducing uncertainty in the varactor capacitance values, the average capacitances values of C_{max} and C_{min} are 0.21639 pF and 0.03258 pF, respectively, and were provided after contacting MACOM. A good agreement was obtained in our previous work between the measurements and the simulations based on the provided average capacitance values [18]. The varactor edges' capacitance values' tolerance was considered in the unit cell's design stage, which minimized its effect. In addition, the varactor has a constant gamma around one, which allows for linear tuning within the reverse bias voltage range of 2 to 12 V [42], as shown in Figure 6.

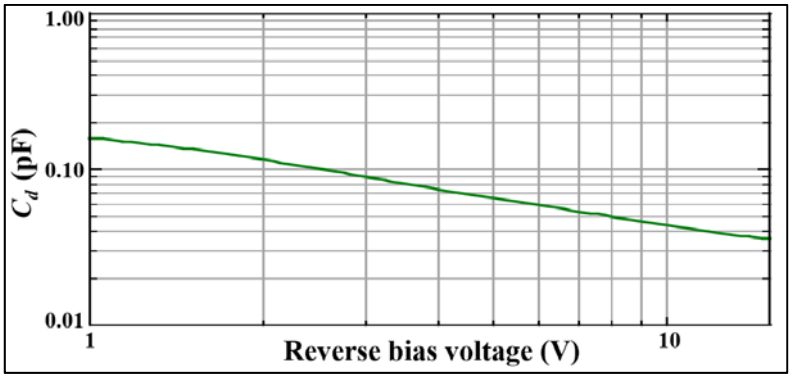

Figure 6. Varactor capacitance values C_d as a function of the reverse bias voltage in log scale.

A prototype based on this unit cell was manufactured. This prototype allowed one-dimensional reflection phase control, where each column was separately stimulated with a DC bias. A photo of the prototype is shown in Figure 7.

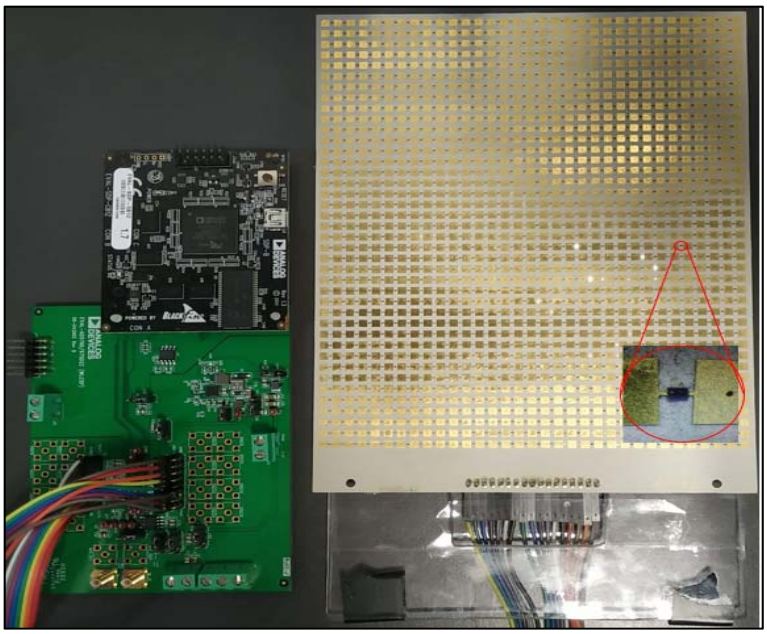

Figure 7. The prototype front side with a zoom-in view on the varactor which is located between each two adjacent unit cells. On the left is the DAC for the DC voltage bias.

Figure 7 shows the manufactured 40-row and 33-column MS, summing up to 1320 unit cells. The MS area sizes were 185 mm $\times$ 140.6 mm ($7.4\lambda_0 \times 6.2\lambda_0$ in wavelength units at 12 GHz).

The design of the MS prototype bottom layer, which functioned as the varactor DC biasing layer, is shown in Figure 8 with a reduced number of lines for convenience.

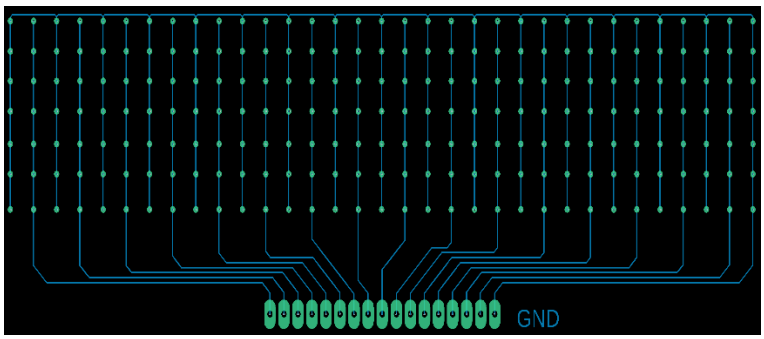

Figure 8. Scheme of a varactor DC biasing layer.

The vias (shown in green) were shortened by vertical DC lines for each unit cells column on the prototype biasing layer. Thus, all odd columns were connected to a common DC ground, and each even column was connected to a separate independent DC voltage of V_1 to V_{16}.

The stimulation voltages V_1 to V_{16} to the varactors in each even column were supplied by an inexpensive programmable DAC model AD5766 from Analog Devices, shown in the left part of Figure 7. This DAC has 16 channels with a 12-bit resolution and a dynamic range of 0 to 16 V. The use of a varactor as a tuning method enabled very high capacitance resolution. However, there was a practical limitation on the reflection phase resolution due to the DAC resolution, which was ΔDC = 3.9 mV.

4. Unit Cell Simulations and Experimental Results

The proposed unit cell properties and the MS reflection were simulated using the TEM Floquet port with 3-D electromagnetic simulation software, namely, CST. Reflection simulations of a unit cell for normal incidence were carried out according to the polarization given in Figures 2 and 5b.

For the more accurate simulation in the 3-D simulated model, the rectangular dielectric slab with the varactor package size, shown in Figure 5a,b in green, was defined with an effective varactor package dielectric constant ε_{eff}. The value of the effective dielectric constant was $\varepsilon_{eff} = 6$ based on our previous work, with a good agreement to the experimental results [18].

The dissipation resistivity of the unit cell R was composed of R_{diel} and R_{ohm}, which were the intrinsic dielectric and ohmic losses, respectively; R_S, which was the varactor serial resistance; and R_P, which related to inaccuracies and parasitics in the manufacturing process. The values of R_{diel} and R_{ohm} were well defined and quantified in CST simulation, while the R_S value was not provided in the datasheet, and the R_P value depends on the manufacturing process quality and not only on the unit cell's inherent properties.

The MS experimental measurements were carried out using two wideband 4 to 40 GHz, double-ridge horn antennas, model PowerLOG 40400, from the Aaronia Company. The two antennas were placed at about 60 cm perpendicular to the MS, one as a transmitter Tx and the other as a receiver Rx. The Tx and Rx antennas were connected to a Vector Network Analyzer (VNA) from the Keysight Company, model P9375A. The measurement setup is shown in Figure 9.

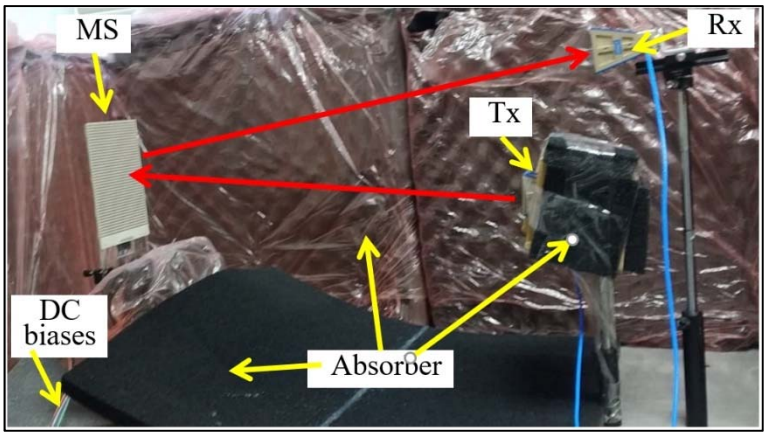

Figure 9. The reflection measurement setup.

Figure 9 shows the measurement setup with the arrangement of the antennas and the MS prototype. The Tx's vertical height was lowered and tilted relative to the MS center. The Rx's vertical height was raised and tilted relative to the MS center to avoid radiation blockage between the Tx and the Rx.

The MS columns were uniformly set with DC voltage or capacitance values for extracted unit cell reflection properties. The unit cell reflection simulation results for the max and min capacitance values compared to the measurement results for 0 V and 16 V reverse bias voltages are shown in Figure 10.

In Figure 10, the unit cell reflection simulation results as a function of frequency in dashed lines for C_{max} = 0.216 pF and C_{min} = 0.033 pF were compared to the measurement results in continuous lines for varactors reverse bias voltages of 0 V and 15 V, respectively. The MS reflection results were normalized to a copper plane surface reflection of the same size. The MS reflection results were normalized to a copper plane surface reflection of the same size. The f_{res} value could be controlled along the entire X-band and the low Ku-band from 7.8 to 15 GHz, depending on the C_d, providing an almost 100% f_{res} tuning and maximum dynamic reflection phase range of 323° and over 300° in the entire X-band.

Thus, the MS reflection allowed for wide bandwidth and significant continuous change in the reflection phase.

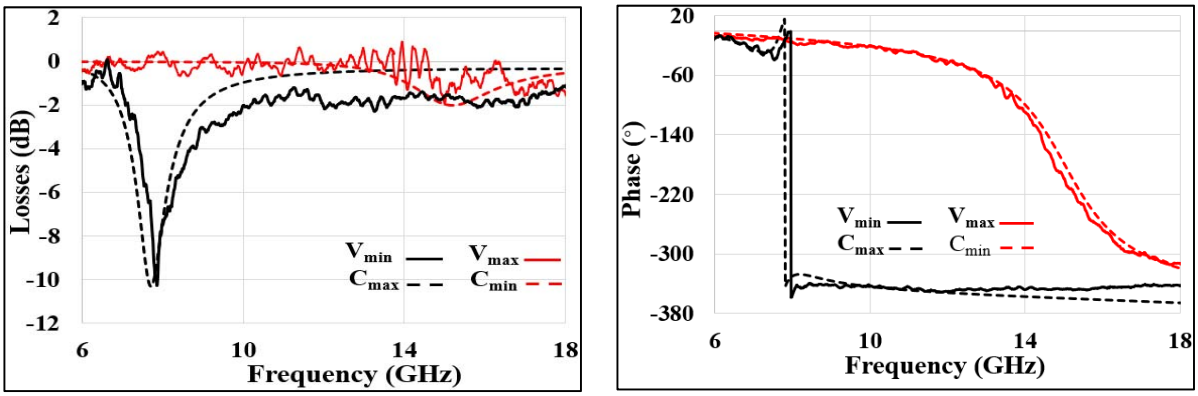

Figure 10. Unit cell reflection measurement and simulation results in continuous lines and dashed lines, respectively: (**a**) reflection magnitude and (**b**) reflection phase.

The resistance values of $R_S + R_P$ were considered in the simulation for each C_d value. The values of $R_S + R_P$ in the simulation results were 19 Ω and 10.5 Ω for C_{max} and C_{min}, respectively. The simulation results showed good agreement with the measurement results. Furthermore, compared to our previous work with the same varactor diode in which the $R_S + R_P$ values were about 7.5 Ω for all C_d capacitance values [18] and compared to another work where the resistance value was 8.5 Ω based on the panel [46], it was shown that not all the measured resistance was related to the varactor, namely, R_S.

This strengthened our decision to define two different resistance components, namely, R_S and R_P, separately. The R_P resistance component depends on the production, frequency, unit cell structure, and MS panel. These two resistance values were extracted as a sum of $R_S + R_P$ in the measurements, making it difficult to determine their values separately.

The reflection simulation results compared to the measurement results for f_{res} around the operating frequencies of 11 GHz, 12 GHz, and 13.5 GHz are shown in Figure 11.

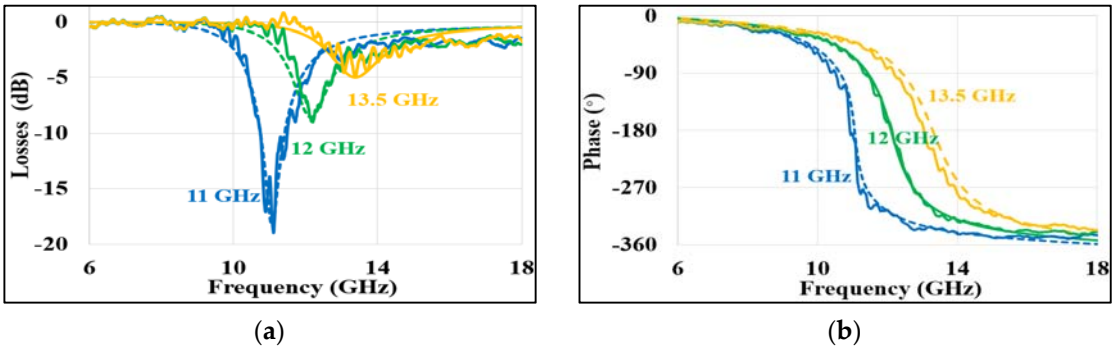

Figure 11. Unit cell reflection measurement and simulation results in continuous lines and dashed lines, respectively: (**a**) reflection magnitude and (**b**) reflection phase.

The unit cell reflection measurement results for the varactor's reverse bias voltages of 2.5 V, 4 V, and 6 V were compared to the simulation results in solid lines for Cd capacitance values of 0.09 pF, 0.069 pF, and 0.052 pF, respectively. The simulation values of $R_S + R_P$ were 17 Ω, 14.8 Ω, and 13.6 Ω for f_{res} around 11 GHz, 12 GHz, and 13.5 GHz, respectively. The measurement results showed good agreement with the simulation results. As C_d decreased, the absorption became smaller and wider, and the reflection phase changed around the f_{res} become moderated, as shown in Figures 10 and 11. These changes resulted

from increasing the bandwidth and decreasing Q according to Equations (4) and (5) . The absorption intensity of the resonance at the working frequency represented the maximum absorption for the working frequency. Therefore, an increase in the working frequencies reduced the losses, as shown in Figure 11a.

5. Unit Cell Reflection Calibration Results

To obtain the dynamic reflection phase calibration curve, all the MS columns were biased uniformly with the same DC voltage values (or capacitance values). The measurement and simulation results of the reflection phase calibration curves, which linked the varactor DC reverse bias or the C_d values to the reflection phase at the operating frequency for three working frequencies, are shown in Figure 12.

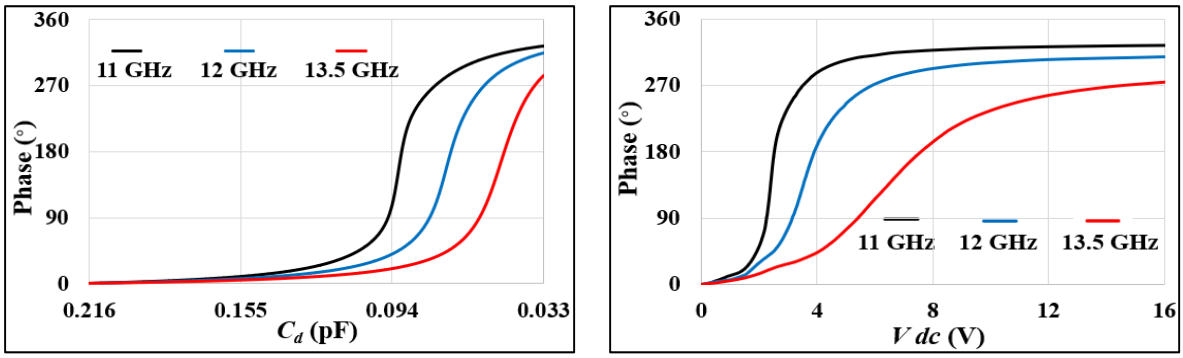

(**a**) (**b**)

Figure 12. Calibration of the reflection phase to the varactor reverse bias for 11 GHz, 12 GHz, and13.5 GHz from left to right, respectively: (**a**) simulation reflection phase calibration results and (**b**) measurement reflection phase calibration results.

The measurements of the dynamic reflection phase were in good agreement with the simulation results for the measured operating frequencies.

The measurement and simulation results of the reflected magnitude, as a function of the varactor capacitance C_d and $V\,dc$ values, respectively, for three operating frequencies, are shown in Figure 13.

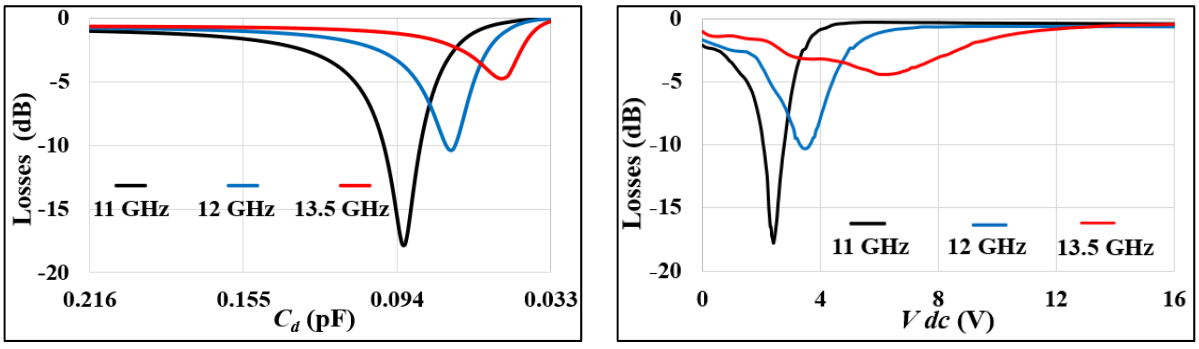

(**a**) (**b**)

Figure 13. Reflection losses as a function of the varactor reverse bias for 11 GHz, 12 GHz, and 13.5 GHz from left to right, respectively: (**a**) reflection losses simulation results and (**b**) reflection losses measurement results.

For higher-frequency operations, the calibration curve became moderated with fewer losses at the expense of decreasing the dynamic phase range, as shown in Figures 12 and 13. Furthermore, for 11 GHz, most of the dynamic capacitance range was acquired in lower absolute values of the DC reverse bias and for 13.5 GHz in higher absolute values. According to the varactor datasheet, about 75% of the total C_d range is enabled for the DC reverse bias range of 0 to 4 V, and the rest obtain for the 4 to 15 V [42]. Thus, additional moderating in

the calibration curves as a function of DC reverse bias will lead to higher steering angle resolution for a high operating frequency.

Since the relation between the varactor reverse bias to the C_d value is not linear, the agreement between the simulation and measurement results in the context of losses is not shown directly from the results curves in Figure 13. Therefore, using post-processing, the measurements and simulations losses as a function of the reflection phase for all operating frequencies were calculated and are shown in Figure 14.

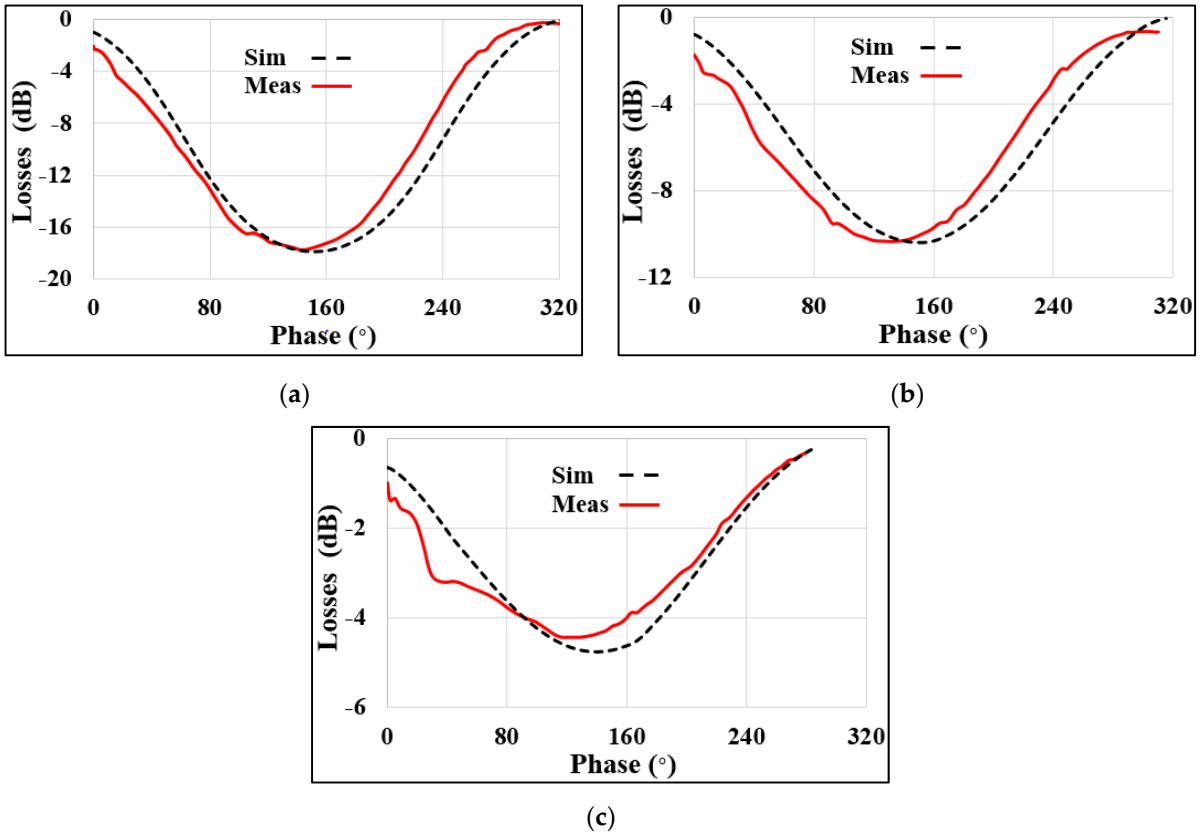

Figure 14. Reflection losses in the operating frequencies as a function of the reflection phase: (**a**) at 11 GHz, (**b**) at 12 GHz, and (**c**) at 13.5 GHz.

The $R_S + R_P$ values for each operating frequency were extracted by comparing the reflection's absorption intensity between the simulations and the measurements (see Figure 11). These $R_S + R_P$ values showed a good agreement in the dynamic phase profile between the measurements and simulations at all operating frequencies.

6. Beam Steering Results

One possible application for this MS type is a reconfigurable steering reflector for radiation, which impinges the MS with polarization, as shown in Figures 2 and 5b. For each operating frequency, the phase calibration curve allows for extracting the appropriate DC reverse biases for each column, which leads to the required phase difference, $\Delta\phi$, between the columns, thus creating the desired phase distribution on the MS reflector for the planned beam steering angle θ as described in Figure 2 and according to Equation (8), where ΔX = 4.2 mm is the unit cell size. The beam steering results at 11 GHz, 12 GHz, and 13.5 GHz for the normal incident are shown in Figure 15.

In Figure 15, for each frequency RCS results set, the black dashed curve is the theoretical upper limit of the steering ability of the relevant frequency. This upper limit is proportional to $cos(\theta)$ [38] and was extracted from the unit cell properties via CST using the active element impedance method [39]. The result for the copper surface in the same

MS size for reference purposes is in the grey curves, and the result for the MS without phase manipulation is in the red curve when both RCS peaks were at angle $\theta = 0°$. The MS beam steering results for several θ angle values, as an example, are in the blue curves. For a planar square reflector, the far-field pattern is proportional to the sinc function. The sinc profile is narrow for a wide size surface and wide for a narrow surface [47]. In this case, the MS reflector size was constant and the wavelengths for each frequency were different; therefore, the profile of the main lobe at 13.5 GHz was narrower than the 11 GHz main lobe, but it depended on the array size rather than an inherent issue.

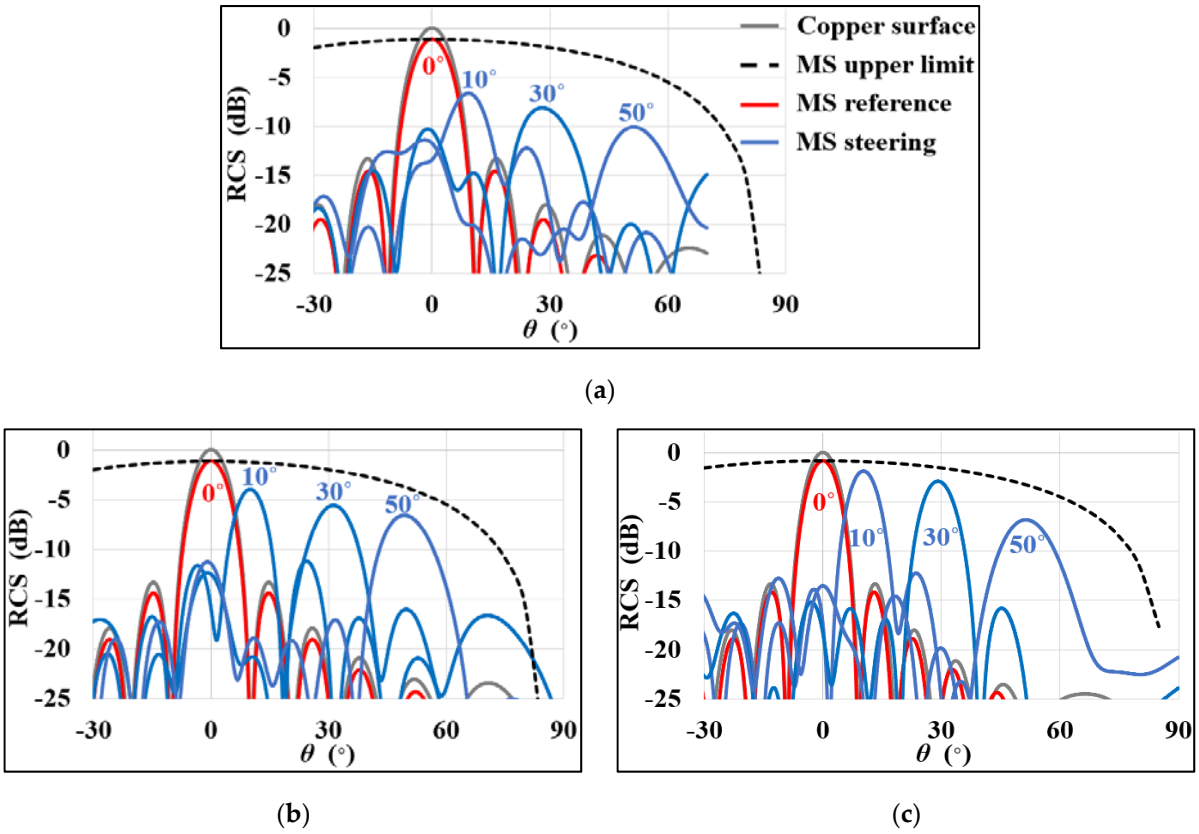

Figure 15. Far-field simulation results for MS reflector: (**a**) at 11 GHz, (**b**) at 12 GHz, and (**c**) at 13.5 GHz.

Tables 1–3 below summarize the steering data and the capability of the beam steering simulation results at 11 GHz, 12 GHz, and 13.5 GHz, respectively. The first row in each table (in italics) is for the copper surface RCS.

Table 1. Parameters for steering angles θ at 11 GHz.

θ Calc/Sim (°)	SLL (dB)	RCS $_{peak}$ (dB)	Efficiency
0°/0°	*13.3*	*0*	*1*
0°/0°	13.4	−1.14	0.767
10°/9.3°	5.58	−6.64	0.217
30°/28.05°	2.17	−8.13	0.154
50°/51.33°	1.31	−10.09	0.098

The steering results improved significantly as the working frequency increased, as shown in Figure 15 and Tables 1–3. The RCS peak of the steering results at 11 GHz was about 5 dB lower than the theoretical upper limit because of the high losses, which were mainly attributed to the diode. This gap closed as the operating frequency increased to

12 GHz and 13.5 GHz. The steering angle in the simulation was very close to the calculated angle, and the efficiency decreased as a function of the steering angle θ.

Table 2. Parameters for steering angles θ at 12 GHz.

θ Calc/Sim (°)	SLL (dB)	RCS $_{peak}$ (dB)	Efficiency
0°/0°	*13.3*	*0*	*1*
0°/0°	13.3	−1.1	0.776
10°/10°	7.23	−3.97	0.4
30°/31.25°	6.76	−5.6	0.276
50°/49.32°	4.7	−6.58	0.22

Table 3. Parameters for steering angles θ at 13.5 GHz.

θ Calc/Sim (°)	SLL (dB)	RCS $_{peak}$ (dB)	Efficiency
0°/0°	*13.3*	*0*	*1*
0°/0°	13.3	−0.83	0.826
10°/10.27°	10.36	−1.89	0.647
30°/29.13°	6.72	−2.92	0.51.1
50°/51.38°	5.93	−6.83	0.275

7. Conclusions

The MS reflector displayed an almost 100% f_{res} tuning performance that covered all of the X-band and half of the Ku-band with a substantial dynamic phase reflection rangeability. The unit cell losses were higher than expected in the preliminary simulation, mainly because the R_S + R_P values were higher in the prototype with measured values higher than 10 Ω. This parameter can be improved by the experience gained in this work with a more accurate manufacturing process. The MS reflector allowed for significant steering ability at 12 GHz and above, as shown in Figure 15 and Tables 2 and 3. These abilities allow for improving satellite communications (QoS) in the X-band and Ku-band.

The design optimization for working frequencies of the MS reflector gave high weight to maximizing the dynamic phase range. In practice, the higher-than-acceptable losses were the main barrier. The simulations showed broad agreement with the measurements for all operating frequencies and capacitance values, indicating that the assumptions regarding the model and the definitions of the simulations were reasonable and valid. The ability to realize an MS reflector at a higher operating frequency based on the tunable mushroom structure is limited. The unit cell C_{int} value reduction, which requires reducing the unit cell sizes, is limited due to the diode located at the front, with its non-negligible size relative to the unit cell area size [17–19]. Reducing the patch size beyond what is done in this work is ineffective regarding reducing the C_{int} [11,36]. Reducing the L_{int} value by reducing the dielectric substrate thickness of the unit cell allows for a significant increase in the operating frequency but, on the other hand, increases the Q and losses and reduces the bandwidth. A substantial increase in the operating frequency for realizing this MS reflector concept without compromising performance and even with improved performance is possible using other geometries [18,19].

Author Contributions: Conceptualization, D.R.; methodology, D.R.; software, D.R.; validation, D.R.; data curation, D.R.; formal analysis, D.R.; investigation, D.R.; resources, D.R. and A.A.; writing—D.R.; writing—review and editing, D.R. and A.A.; visualization, D.R.; supervision, A.A.; project administration, D.R.; funding acquisition, A.A. Both authors have read and agreed to the published version of the manuscript.

Funding: This research received no external funding.

Conflicts of Interest: The authors declare no conflict of interest.

References

1. Li, A.; Singh, S.; Sievenpiper, D. Metasurfaces and their applications. *Nanophotonics* **2018**, *7*, 989–1011. [CrossRef]
2. Bukhari, S.S.; Vardaxoglou, J.Y.; Whittow, W. A metasurfaces review: Definitions and applications. *Appl. Sci.* **2019**, *9*, 2727. [CrossRef]
3. Faenzi, M.; Minatti, G.; González-Ovejero, D.; Caminita, F.; Martini, E.; Della Giovampaola, C.; Maci, S. Metasurface antennas: New models, applications and realizations. *Sci. Rep.* **2019**, *9*, 10178. [CrossRef]
4. Turpin, J.P.; Bossard, J.A.; Morgan, K.L.; Werner, D.H.; Werner, P.L. Reconfigurable and tunable metamaterials: A review of the theory and applications. *Int. J. Antennas Propag.* **2014**, *2014*, 429837. [CrossRef]
5. Quevedo-Teruel, O.; Chen, H.; Díaz-Rubio, A.; Gok, G.; Grbic, A.; Minatti, G.; Martini, E.; Maci, S.; Eleftheriades, G.V.; Chen, M.; et al. Roadmap on metasurfaces. *J. Opt.* **2019**, *21*, 073002. [CrossRef]
6. Smith, D.R.; Padilla, W.J.; Vier, D.C.; Nemat-Nasser, S.C.; Schultz, S. Composite medium with simultaneously negative permeability and permittivity. *Phys. Rev. Lett.* **2000**, *84*, 4184. [CrossRef] [PubMed]
7. Shelby, R.A.; Smith, D.R.; Schultz, S. Experimental verification of a negative index of refraction. *Science* **2001**, *292*, 77–79. [CrossRef]
8. Sievenpiper, D.F.; Schaffner, J.H.; Song, H.J.; Loo, R.Y.; Tangonan, G. Two-dimensional beam steering using an electrically tunable impedance surface. *IEEE Trans. Antennas Propag.* **2003**, *51*, 2713–2722. [CrossRef]
9. Wang, Z.; Liao, D.; Zhang, T.; Chen, T.; Ruan, Y.; Zheng, B. Metasurface-based focus-tunable mirror. *Opt. Express* **2019**, *27*, 30332–30339. [CrossRef] [PubMed]
10. Chaimool, S.; Zhao, Y. Applications of Gradient Metasurfaces: A Review. *ECTI E-Mag.* **2017**, *11*, 3–13.
11. Sievenpiper, D. High-Impedance Electromagnetic Surfaces. Ph.D. Thesis, Department of Electrical Engineering, University California at Los Angeles, Los Angeles, CA, USA, 1999.
12. Asgharian, R.; Zakeri, B.G.; Yazdi, M. A Narrow Beam, Beam Steerable and Low Side-Lobe Reflectarray Based on Macro Electro-Mechanical Technique. *Prog. Electromagn. Res.* **2020**, *100*, 73–82. [CrossRef]
13. Yang, H.; Yang, F.; Xu, S.; Mao, Y.; Li, M.; Cao, X.; Gao, J. A 1-bit 10×10 reconfigurable reflectarray antenna: Design, optimization, and experiment. *IEEE Trans. Antennas Propag.* **2016**, *64*, 2246–2254. [CrossRef]
14. Nie, J.; Tan, Y.Q.; Ji, C.L.; Liu, R.P. Analysis of Ku-Band steerable metamaterials reflectarray with tunable varactor diodes. In Proceedings of the 2016 Progress in Electromagnetic Research Symposium (PIERS), Shanghai, China, 8–11 August 2016; pp. 709–713.
15. Vásquez-Peralvo, J.A.; Fernández-González, J.M.; Rigelsford, J.M. Beam Steering Using Active Artificial Magnetic Conductors: A 10-Degree Step Controlled Steering. *IEEE Access* **2020**, *8*, 177964–177975. [CrossRef]
16. Foo, S. Liquid-crystal-tunable metasurface antennas. In Proceedings of the 2017 11th European Conference on Antennas and Propagation (EUCAP), Paris, France, 19–24 March 2017; pp. 3026–3030.
17. Rotshild, D.; Abramovich, A. Wideband reconfigurable entire Ku-band metasurface beam-steerable reflector for satellite communications. *IET Microw. Antennas Propag.* **2019**, *13*, 334–339. [CrossRef]
18. Rotshild, D.; Abramovich, A. Realization and validation of continuous tunable metasurface for high resolution beam steering reflector at K-band frequency. *Int. J. RF Microw. Comput. -Aided Eng.* **2021**, *31*, e22559. [CrossRef]
19. Rotshild, D.; Rahamim, E.; Abramovich, A. Innovative Reconfigurable Metasurface 2-D Beam-Steerable Reflector for 5G Wireless Communication. *Electronics* **2020**, *9*, 1191. [CrossRef]
20. Cui, T.J.; Qi, M.Q.; Wan, X.; Zhao, J.; Cheng, Q. Coding metamaterials, digital metamaterials and programmable metamaterials. *Light Sci. Appl.* **2014**, *3*, e218. [CrossRef]
21. Huang, C.; Sun, B.; Pan, W.; Cui, J.; Wu, X.; Luo, X. Dynamical beam manipulation based on 2-bit digitally-controlled coding metasurface. *Sci. Rep.* **2017**, *7*, 42302. [CrossRef] [PubMed]
22. Momeni Hasan Abadi, S.M.A.; Booske, J.H.; Behdad, N. MAcro-Electro-Mechanical Systems (MÆMS) based concept for microwave beam steering in reflectarray antennas. *J. Appl. Phys.* **2016**, *120*, 054901. [CrossRef]
23. Yaghmaee, P.; Karabey, O.H.; Bates, B.; Fumeaux, C.; Jakoby, R. Electrically tuned microwave devices using liquid crystal technology. *Int. J. Antennas Propag.* **2013**, *2013*, 824214. [CrossRef]
24. Solderable AlGaAs Flip Chip PIN. Available online: https://cdn.macom.com/datasheets/MADP-000907-14020x.pdf (accessed on 15 June 2021).
25. Kamoda, H.; Iwasaki, T.; Tsumochi, J.; Kuki, T. 60-GHz electrically reconfigurable reflectarray using pin diode. In Proceedings of the 2009 IEEE MTT-S International Microwave Symposium Digest, Boston, MA, USA, 7–12 June 2009; pp. 1177–1180.
26. Tian, W.; Li, P.; Yuan, L. Research and analysis of MEMS switches in different frequency bands. *Micromachines* **2018**, *9*, 185. [CrossRef]
27. Naito, Y.; Nakamura, K.; Uenishi, K. Laterally movable triple electrodes actuator toward low voltage and fast response RF-MEMS switches. *Sensors* **2019**, *19*, 864. [CrossRef]
28. Hand, T.H.; Cummer, S.A. Reconfigurable reflectarray using addressable metamaterials. *IEEE Antennas Wirel. Propag. Lett.* **2010**, *9*, 70–74. [CrossRef]
29. Xu, H.X.; Tang, S.; Ma, S.; Luo, W.; Cai, T.; Sun, S.; He, Q.; Zhou, L. Tunable microwave metasurfaces for high-performance operations: Dispersion compensation and dynamical switch. *Sci. Rep.* **2016**, *6*, 38255. [CrossRef]
30. Ratni, B.; de Lustrac, A.; Piau, G.P.; Burokur, S.N. Active metasurface for reconfigurable reflectors. *Appl. Phys. A* **2018**, *124*, 104. [CrossRef]

31. MACOM. MAVR-000120-1141, Solderable GaAs Constant Gamma Flip-Chip Varactor Diode. Available online: https://cdn.macom.com/datasheets/MAVR-000120-1411.pdf (accessed on 15 June 2021).
32. Du, B. Analysis and Design of Simple, Low Loss and Low Cost Reconfigurable Reflectarrays. Ph.D. Thesis, University of Toronto, Toronto, ON, Canada, 2017.
33. Han, J.; Li, L.; Liu, G.; Wu, Z.; Shi, Y. A wideband 1 bit 12 × 12 reconfigurable beam-scanning reflectarray: Design, fabrication, and measurement. *IEEE Antennas Wirel. Propag. Lett.* **2019**, *18*, 1268–1272. [CrossRef]
34. Popov, V.; Ratni, B.; Burokur, S.N.; Boust, F. Non-Local Reconfigurable Sparse Metasurface: Efficient Near-Field and Far-Field Wavefront Manipulations. *Adv. Opt. Mater.* **2021**, *9*, 2001316. [CrossRef]
35. Chattopadhyay, J.; Rao, S.S. Task identification in Massive MIMO Technology for Its Effective Implementation in 5G and Satellite Communication. In Proceedings of the 2020 International Conference on Communication and Signal Processing (ICCSP), Chennai, India, 28–30 July 2020; pp. 268–271.
36. Rea, S.P.; Linton, D.; Orr, E.; McConnell, J. Broadband high-impedance surface design for aircraft HIRF protection. *IEE Proc. -Microw. Antennas Propag.* **2006**, *153*, 307–313. [CrossRef]
37. Pozar, D.M. *Microwave Engineering*; John Wiley & Sons: Hoboken, NJ, USA, 2001.
38. Bhattacharyya, A.K. *Phased Array Antennas: Floquet Analysis, Synthesis, BFNs and Active Array Systems*; John Wiley & Sons: Hoboken, NJ, USA, 2006; Volume 179.
39. Rütschlin, M.; Wittig, T.; Iluz, Z. Phased antenna array design with CST STUDIO SUITE. In Proceedings of the 2016 10th European Conference on Antennas and Propagation (EuCAP), Davos, Switzerland, 10–15 April 2016; pp. 1–5.
40. Ghasemifard, F.; Norgren, M.; Quevedo-Teruel, O. Dispersion analysis of 2-D glide-symmetric corrugated metasurfaces using mode-matching technique. *IEEE Microw. Wirel. Compon. Lett.* **2017**, *28*, 1–3. [CrossRef]
41. Rogers Corporation. RT/Duroid®5880LZ. Available online: https://www.rogerscorp.com/-/media/project/rogerscorp/documents/advanced-connectivity-solutions/english/data-sheets/rt-duroid-5880lz-high-frequency-laminates.pdf (accessed on 15 June 2021).
42. MACOM. MAVR-011020-1411, Solderable GaAs Constant Gamma Flip-Chip Varactor Diode. Available online: https://cdn.macom.com/datasheets/MAVR-011020-1141.pdf (accessed on 15 June 2021).
43. Gao, X.; Zhang, J.; Zhang, H.C.; Liu, L.; Ma, Q.; Xu, P.; Cui, T.J. Dynamic Controls of Second-Harmonic Generations in Both Forward and Backward Modes Using Reconfigurable Plasmonic Metawaveguide. *Adv. Opt. Mater.* **2020**, *8*, 1902058. [CrossRef]
44. Waterlot, G.; Craeye, C.; Oestges, C. Optimisation des Antennes-Relais en vue de Réduire L'exposition Humaine aux Ondes Electromagnétiques dans les Réseaux Cellulaires. Master's Thesis, Ecole Polytechnique de Louvain, Université Catholique de Louvain, Leuven, Belgium, 2020.
45. Xu, M.Y. Reconfigurable Dual-band and Wide-band Spatially-fed Array Antennas. Ph.D. Thesis, University of Toronto, Toronto, ON, Canada, 2020.
46. Popov, V.; Ratni, B.; Burokur, S.N.; Boust, F. Supplementary Information Non-local reconfigurable sparse metasurface: Efficient near-field and far-field wavefront manipulations. *Adv. Opt. Mater.* **2021**, *9*, 2001316. [CrossRef]
47. Tyson, R.K. *Principles and Applications of Fourier Optics*; IOP Publishing: Bristol, UK, 2014.